Flow Investigations in a Stalling Nacelle Inlet

Simon Übelacker[1,*], Rainer Hain[1], Christian J. Kähler[1]

1: Institute of Fluid Mechanics and Aerodynamics, Universität der Bundeswehr München, 85577 Neubiberg, Germany
* correspondent author: simon.uebelacker@unibw.de

Abstract A flow-through nacelle was investigated at the Institute of Fluid Mechanics and Aerodynamics of the Universität der Bundeswehr in Munich. The boundary layer loading of the nacelle resembles that of a powered engine at take-off conditions and high mass flow rates, see Schulze (2013). The aim of the project is to generate an experimental validation database in order to develop a physically based numerical code to calculate the flow at the edge of the flight envelope. The investigations concentrated on the flow under an inhomogeneous onstream. Therefore, a vortex generator was positioned 1.74 m in front of the nacelle's leading edge. This vortex generator is a motor driven airfoil, which pitches from angles of attack of α_{vg} = -11° to α_{vg} = 11° within approximately 60 ms.

1. Introduction

In a time of increasing air traffic, reliable numerical codes for the calculation of wing and nacelle stall are required. Moreover, the expansion of the flight envelope's edge has recently been a challenging task for the industry and the engineering sciences. The Deutsche Forschungsgemeinschaft Research Group 1066 "Simulation of Wing and Nacelle Stall" is developing different numerical codes for the flight at the edge of the aircraft's envelope. A general overview about this work is given in Radespiel et al. (2013) and Niehuis et al. (2013).

Validation experiments are required for the development of numerical models. Therefore, a cold flow-through nacelle was developed and investigated at the Institute of Fluid Mechanics and Aerodynamics at the Universität der Bundeswehr München. Recent investigations focused on the start and landing period of the aircraft (i.e. low speed and high angles of attack). During this phase of flight a turbulent separation bubble develops in the front part of the intake. Figure 1 shows the pressure distribution in the inlet of the examined model. The pressure coefficient c_p is plotted against the x-coordinate in the main flow direction. The static pressure is measured in the inner mid section of the nacelle between 0 and 60% of the chord. While at α_n = 19° the boundary layer is still attached, at α_n = 23° a turbulent separation has formed. The separated region is characterized by the plateau of the pressure.

This separation is a highly unsteady phenomenon. Vortices develop and are shed downstream. Therefore, an interaction with the compressor is likely. A vortex can hit the blade and locally change the angle of attack of

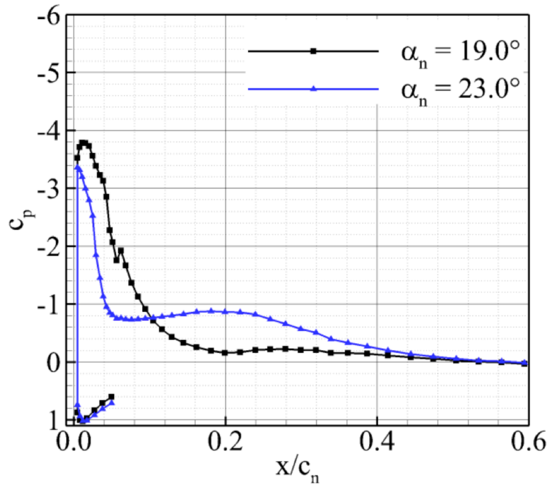

Fig. 1 Pressure distribution in the inlet

the blade. This can cause stall to the compressor. Stall or rotating stall leads to total pressure losses in the compressor. The total pressure loss decreases the efficiency of the compression stage of the engine. Moreover, the vortex shedding can cause blade vibrations. These vibrations can lead to material failure of the jet-engine.
Additionally, atmospheric turbulence is relevant when the airplane is flying close to the ground. Gusts can hit the inlet and interact or even cause the separation. The aim of this work was to investigate the interaction of a generic vortex with the flow and the separation in the inlet.

2. Experimental setup

A cold flow-through nacelle was used for the investigations, see Fig. 2 (a). The axially symmetric model has a chord length of c_n = 526 mm and a leading edge diameter of 315.6 mm. The nacelle was developed on the basis of the Laminar Flow Research Action (LARA) nacelle, see Schulze et al. (2007).
As the experiments were performed at a relatively low onflow Mach number $Ma = 0.11$, the separation is not shock induced as in the LARA nacelle. However, the shape of the inner side of the nacelle was modified in order to achieve a pressure induced separation, see Schulze (2013). The front part of the model is made from Plexiglas® to allow for optical access, whereas the rear part, which connects the model with the sting, is made from steel.
All presented experiments were performed at a Reynolds number of $Re_{cn} \approx 1.25 \cdot 10^6$. The Reynolds number is based on the chord length of the nacelle. The experiments were conducted at the atmospheric wind tunnel Munich. This facility is an Eiffel-type wind tunnel with a closed test section. The dimensions of the test section are 1.85 m x 1.85 m x 20 m. The maximum velocity of this facility is U_∞ = 40 m/s. Conventional static pressure measurements were performed in order to find the angle of attack with separation onset. It became apparent that separation occurs at $\alpha_n \approx 21°$.
The investigations focused on the interaction between the inlet stall and the inhomogeneous onstream. Flow distortions can occur while the airplane is flying through gusty conditions. The distortions can be critical at the edge of the flight envelope. In order to generate a gust in the wind tunnel, a distortion generator was developed, see Hahn et al. (2012). This vortex generator is a pitching airfoil, which was positioned 1.74 m upstream of the nacelle, see Fig. 2 (a). Two linear motors on each side are moving the airfoil from outside the wind tunnel. The airfoil is a NACA 0021 with a chord length of c_{vg} = 160 mm. The airfoil's shell is made from carbon fiber laminate. The vortex generator moves from α_{vg} = -11° to α_{vg} = 11° within 60 ms, pauses at approximately α_{vg} = 11° for 195 ms, moves back to α_{vg} = -11° within 79 ms, and pauses at α_{vg} = -11° for approximately 168 ms. Figure 2 (b) shows the angle of attack of the vortex generator over time. These data are acquired with a potentiometer. The plot shows that one cycle lasts 500 ms. By moving from α_{vg} = -11° to α_{vg} = 11°, a counter clockwise rotating vortex was generated in the test section. In this investigation, the interaction of the turbulent separation bubble with this counter clockwise rotating vortex was of main

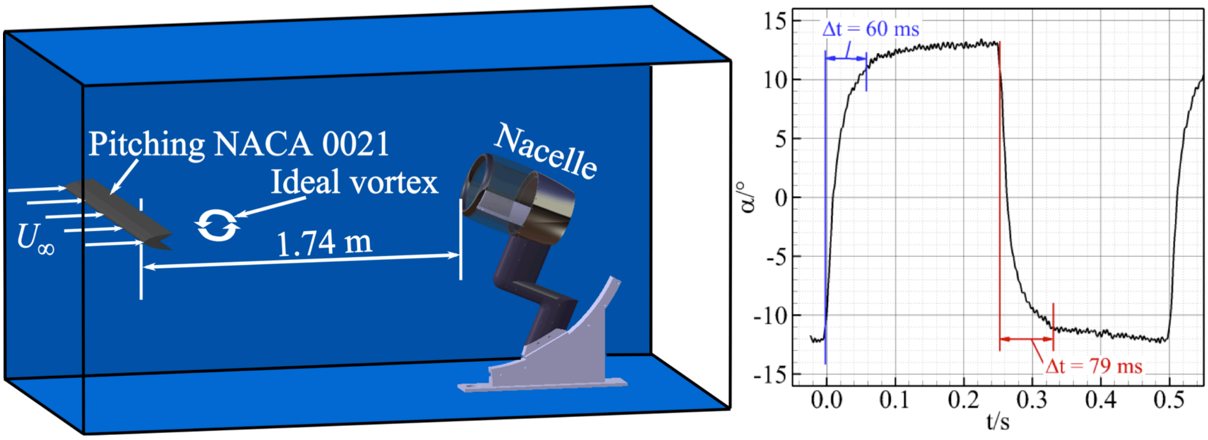

(a) Experimental Setup **(b)** Pitch of the vortex generator
Fig. 2 Experimental setup with the vortex generator 1.74 m upstream of the nacelle (left). Potentiometer data of the pitching airfoil (right)

(a) Light sheet in main flow direction **(b)** Light sheet perpendicular to the *x*-axis

Fig. 3 Complementary light sheets

interest. This vortex is considered critical due to the fact that it primarily increases the angle of attack of the nacelle before the angle of attack is reduced.

In order to achieve an interaction of the convecting vortex and the turbulent separation bubble, the airfoil of the vortex generator was mounted at a height of 950 mm from the ground of the wind tunnel. In the investigated range of the nacelle's angle of attack (between $\alpha_n = 19°$ and $\alpha_n = 23°$), the leading edge of the nacelle has also a height of approximately 950 mm from the ground, see Fig. 2 (a). Therefore, the vortex is expected to impinge the nacelle close to the leading edge.

The presented measurement techniques are static pressure measurements, see Fig. 1, and Stereoscopic Particle Image Velocimetry (SPIV). Besides, time resolved pressure measurements in the inlet were performed in order to acquire the fluctuations of the static pressure as well as to detect the interaction between the vortex and the nacelle. Furthermore, threads were attached in the region of the turbulent separation bubble to determine the symmetry of the flow in the intake. The results of the latter method indicate that in the majority of the cases the flow can be considered symmetrical.

For the mentioned SPIV experiments two high-speed CMOS Cameras (Imager pro HS 4M) were installed above the test section at a distance of approximately 1.3 m from the field of view. The spatial resolution is reduced to 2016 px x 704 px. At this resolution a maximum, frame rate in the double frame mode of this camera - as it is required for conventional PIV - was 1800 Hz. In this mode, the camera acquires single images with twice the frequency (i.e. 3600 Hz).

The maximum frequency was exploited in these measurements only to acquire a single cycle of the vortex generator (500 ms) in order to achieve the maximum time resolution. However, the SPIV results presented in this paper correspond to data acquired at a frame rate of 1000 Hz and 500 Hz in the double frame mode. The measurements in the plane along the main direction of the flow were conducted with the higher frame rate, whereas the measurements in the plane perpendicular to the roll axis (*x*-axis) of the nacelle were performed with the lower frame rate. The reduction of the frame rate is done to shorten the transfer time of the data from the internal memory of the camera to the computer. Moreover, the measurements at steady state of the vortex generator in both sections were acquired at 100 Hz in the double frame mode in order to increase the measurement time.

The first measurement plane is located in the mid section of the axially symmetric nacelle. The laser light sheet was inserted into the nacelle from downstream, see Fig. 3 (a). The measurement plane perpendicular to the *x*-axis was positioned at 20% of the chord length behind the leading edge of the nacelle. At $\alpha_n = 23°$, this section was considered to be in the separation region, see Fig. 1. With the perpendicular measurement plane, it was expected to get information of the spanwise scales of the turbulent separation bubble. Therefore, the laser light sheet was set through the Plexiglas® of the nacelle, see Fig. 3 (b). The light sheet thickness was 2 mm to 3 mm. A Zeiss Makro Planar T*2/100 lens was used. The SPIV validations were carried out with a decreasing window size from 64 px to 32 px and 50% interrogation window overlap.

The trigger signal was set when the vortex generator was passing $\alpha_{vg} = -10°$. The measurement was started with a short delay of 12 ms to 33 ms and 30 images - 105 images were acquired. This cycle was repeated 1000 times. Therefore, 1000 vector fields were averaged for consecutive times after the trigger signal. The

time delay and the number of acquired images were chosen to guarantee sufficient time to record the vortex convecting through the nacelle.
The presented results are for $\alpha_n = 19°$ and for $\alpha_n = 23°$. Therefore, the attached case as well as the separated angle of attack will be discussed, see Fig. 1.

3. Results

Due to the change in angle of attack of the symmetric airfoil of the vortex generator, a vortex develops and is convected downstream. Former planar PIV measurements indicate that a vortex (visualized by the d_2-criterion) actually develops, see Fig. 4. This criterion separates vortices from other patterns, see Vollmers (2001). Figure 4 shows the wake of the vortex generator at the position of the nacelle but without the nacelle in the wind tunnel. The origin of the Cartesian coordinate system is the bottom leading edge of the nacelle with x pointing downstream along the roll-axis of the nacelle and z pointing up, see Fig. 5. In Fig. 4, the freestream velocity was subtracted from the vector field. The colored area shows the relevant values of the d_2-criterion. Without the nacelle in the test section no significant shift of the height of the convecting vortex is observed.

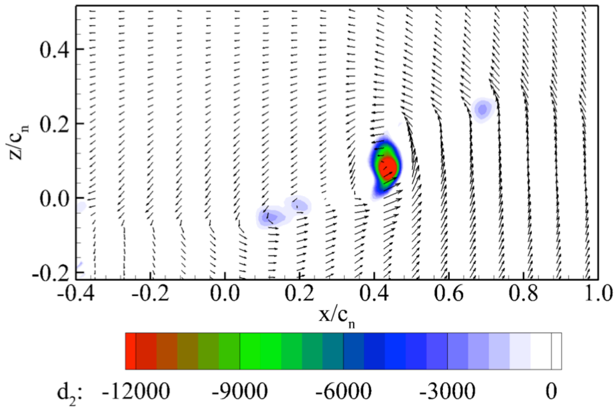

Fig. 4 Wake of the vortex generator

In Figs. 5 - 8 the averaged absolute flow field is shown. Figures 5 and 6 show the image section in the main flow direction at the nacelle's bottom leading edge (black), whereas Figs. 7 and 8 show the mean vector field for the cross section. Figures (a) display the result for the time $t = 34$ ms after the trigger signal of the vortex generator, whereas Figs. (b) illustrate the vector field for the time $t = 60$ ms after the trigger signal. The time was counted from the airfoil passing $\alpha_{vg} = -10°$, see Fig. 2 (b). In Figs. 5 and 7 the angle of attack of the nacelle is $\alpha_n = 19°$ and in Figs. 6 and 8 the angle of attack is $\alpha_n = 23°$. Note the different color scaling of the absolute mean velocities in Figs. 5, 6 and Figs. 7, 8.
The absolute velocity in the plane of the main flow direction is given as

$$|U_{xz}|/U_\infty = \sqrt{(u/U_\infty)^2 + (w/U_\infty)^2}, \tag{1}$$

whereas the absolute velocity in the cross section is

$$|U_{yz}|/U_\infty = \sqrt{(v/U_\infty)^2 + (w/U_\infty)^2}. \tag{2}$$

While, u is the velocity component in the x-direction, v is the component of the velocity in the y-direction and w the velocity in the z-direction. All velocity vectors are averaged over 1000 vector fields.
In Fig. 5, it becomes apparent that the absolute velocity at the leading edge is higher compared to $\alpha_n = 23°$ in Fig. 6. This results in a higher suction peak and is shown in Fig. 1. Figure 6 (b), when $t = 60$ ms, also shows that the separation is slightly bigger compared to $t = 34$ ms. This is indicated with the bigger blue area, which

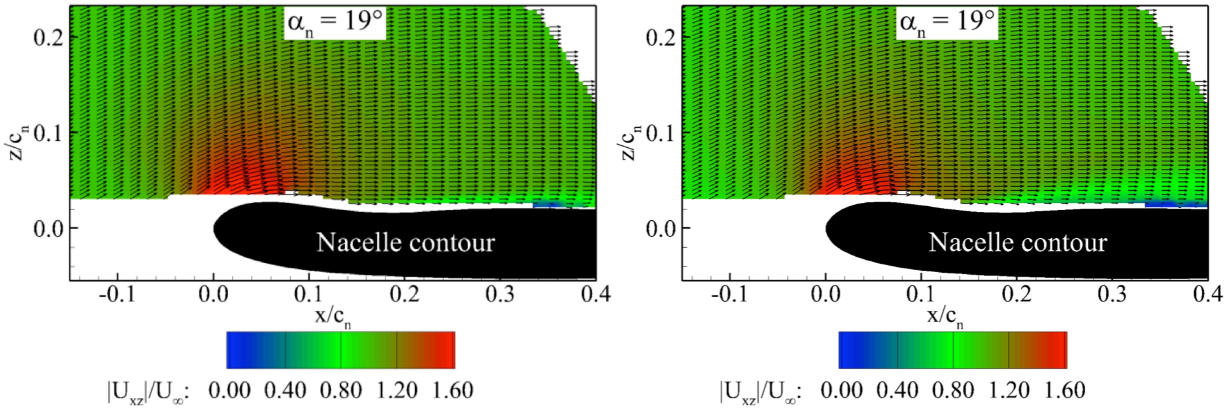

(a) t = 34 ms **(b)** t = 60 ms

Fig. 5 Mean in-plane flow field at α_n = 19°, light sheet in flow direction

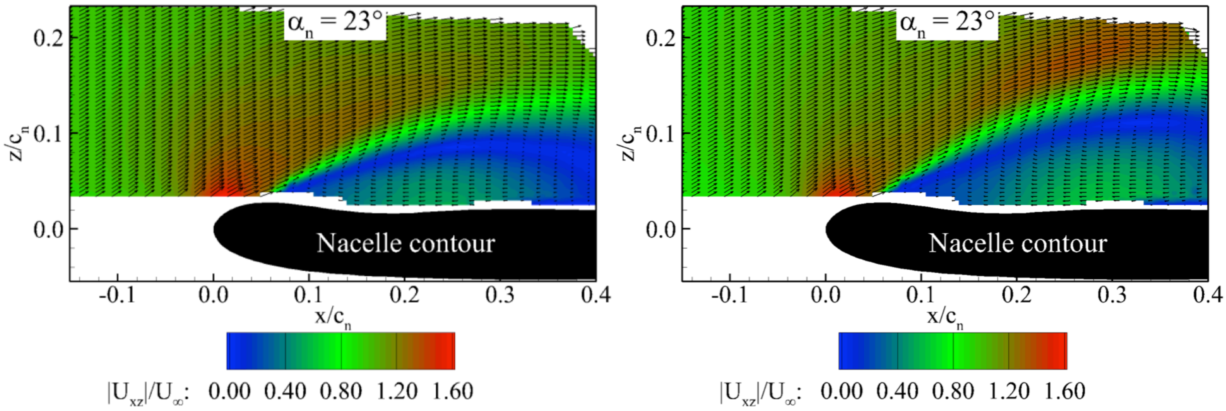

(a) t = 34 ms **(b)** t = 60 ms

Fig. 6 Mean in-plane flow field at α_n = 23°, light sheet in flow direction

shows an area of low absolute velocities. At an angle of attack of α_n = 19° the velocities are decelerated as well at t = 60 ms. This is indicated by a bright green area downstream of the leading edge close to the wall in Fig. 5 (b).

In the cross section, the absolute in-plane velocity component far from the wall is higher at α_n = 23°, see Fig. 8, compared with the lower angle of attack in Fig. 7. On the one hand, at the higher angle of attack some time later the absolute velocity is higher. On the other hand, at α_n = 19° the velocity in the center of the nacelle seems to decelerate. Figure 8 (a) also shows that the blue region of low velocities is not symmetrical. This asymmetry was also observed at other times before the vortex reaches the nacelle and was shown before with oil flow measurements, see Schulze (2013). Figures 9 - 12 show the normalized turbulent kinetic energy for the same angles of attack and the corresponding times of Figs. 5 - 8. The arrangement of the Figs. 9 - 12

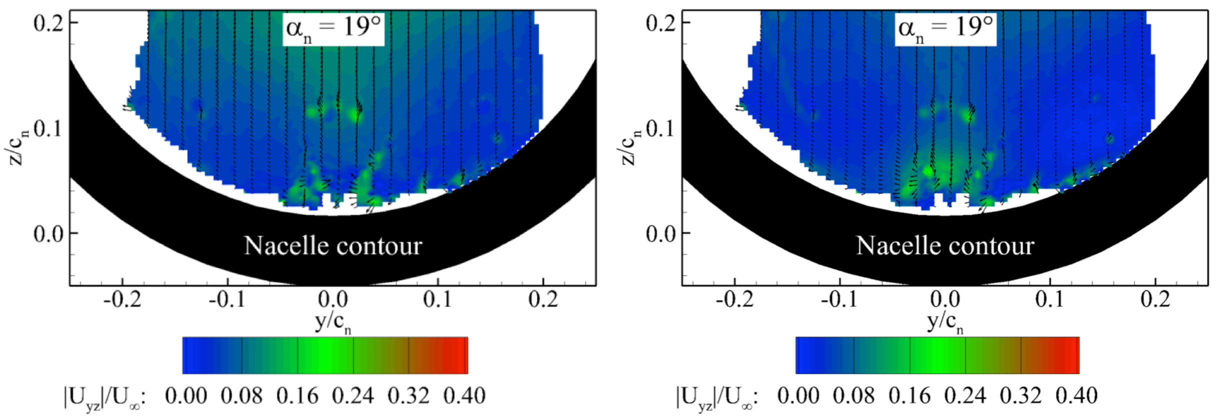

(a) t = 34 ms **(b)** t = 60 ms

Fig. 7 Mean in-plane flow field at α_n = 19°, light sheet perpendicular to the flow direction

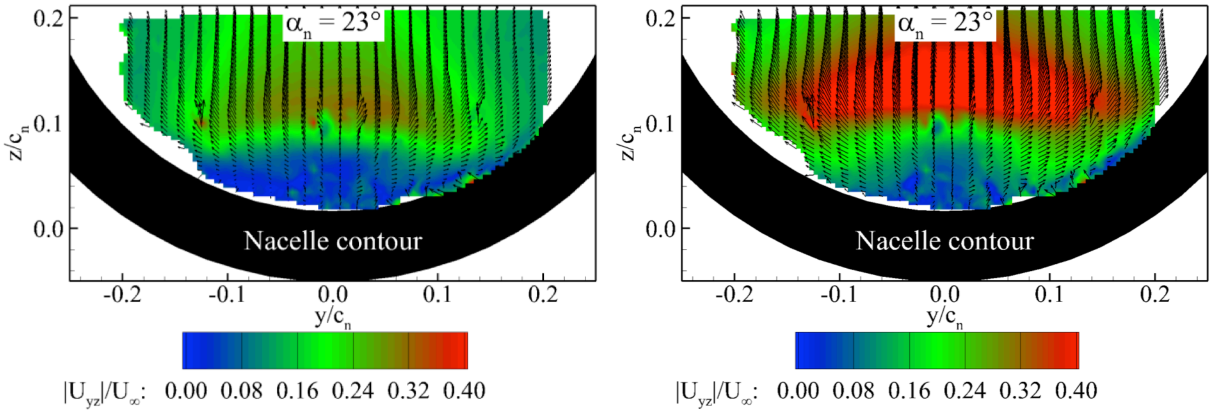

(a) $t = 34$ ms **(b)** $t = 60$ ms

Fig. 8 Mean in-plane flow field at $\alpha_n = 23°$, light sheet perpendicular to the flow direction.

is consistent with the Figures above. Due to the equal scaling, it can be clearly seen that the level of turbulent kinetic energy is relatively high at $\alpha_n = 23°$ compared to $\alpha_n = 19°$. This is a result of the separated flow at the higher angle of attack.

At time $t = 60$ ms it is also apparent that the fluctuations of the three velocity components are higher than at $t = 34$ ms. This result indicates that the counter clockwise rotating vortex enlarges the fluctuations in the flow. If the separation is already present, the separated region will also be increased. This increase of the separated region is not only valid for the main flow direction, see Fig. 10, but also for the spanwise direction in Fig. 12. Therefore, the impact of the distortion on the flow through the nacelle is considered to be significant and to destabilize the flow in the intake.

Fig. 2 (a) shows that the vortex generator's trailing edge was placed 1.74 m upstream of the nacelle's leading

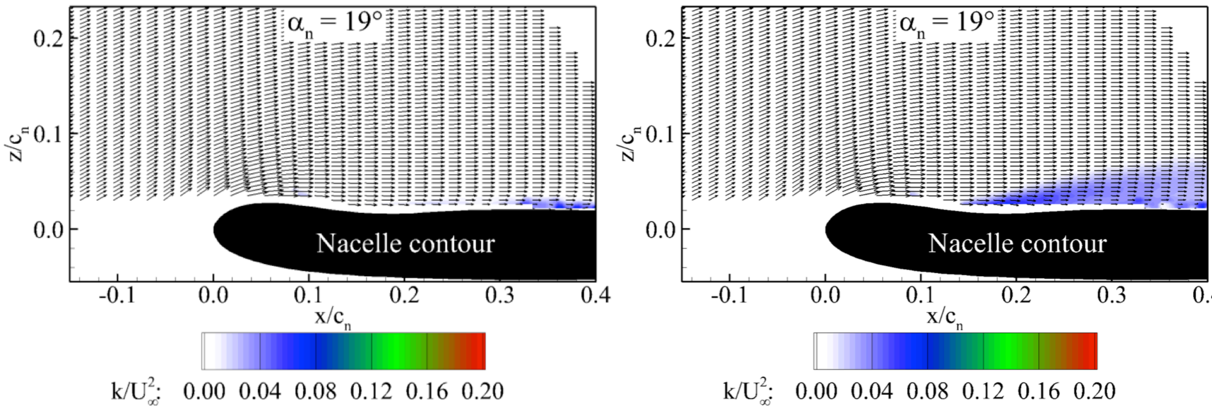

(a) $t = 34$ ms **(b)** $t = 60$ ms

Fig. 9 Normalized turbulent kinetic energy at $\alpha_n = 19°$, light sheet in flow direction

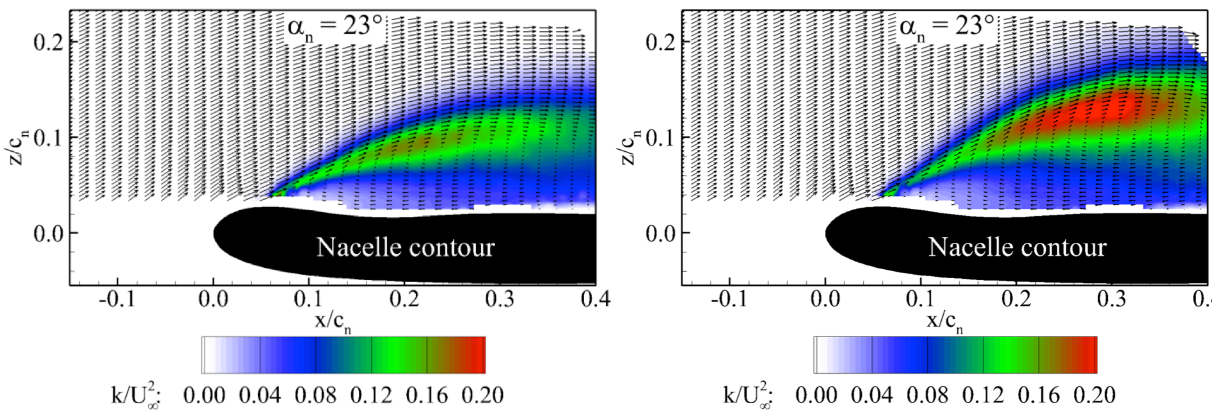

(a) $t = 34$ ms **(b)** $t = 60$ ms

Fig. 10 Normalized turbulent kinetic energy at $\alpha_n = 23°$, light sheet in flow direction

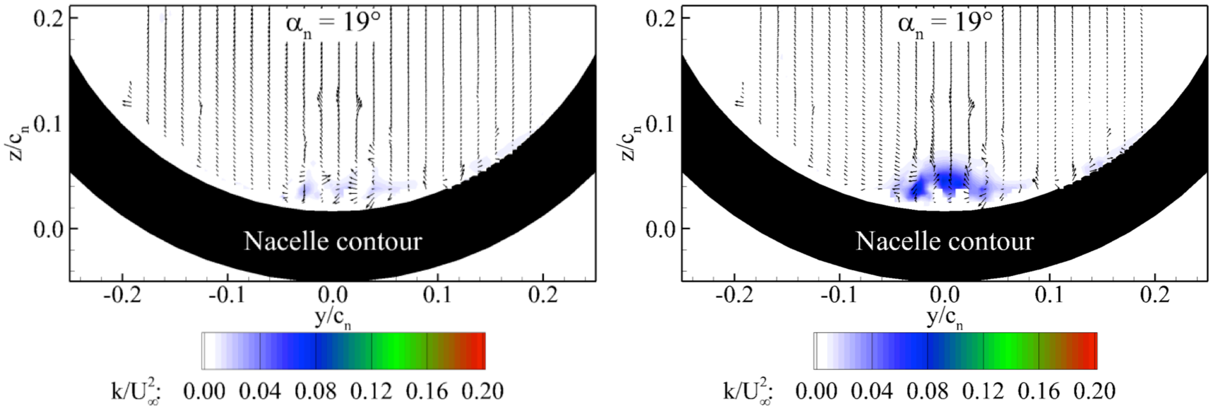

(a) t = 34 ms **(b)** t = 60 ms

Fig. 11 Normalized turbulent kinetic energy at α_n = 19°, light sheet perpendicular to the flow direction

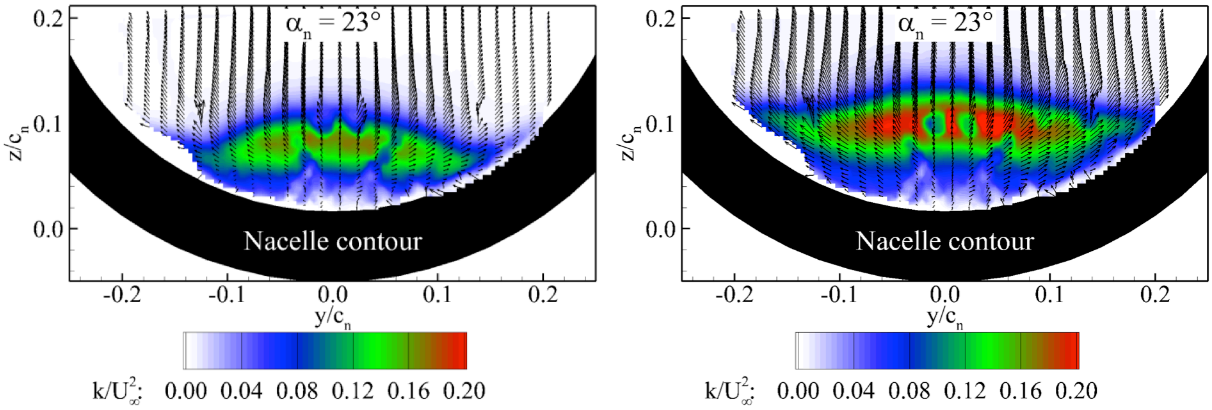

(a) t = 34 ms **(b)** t = 60 ms

Fig. 12 Normalized turbulent kinetic energy at α_n = 23°, light sheet perpendicular to the flow direction

edge. The convection time of the vortex between the vortex generator and the nacelle is expected to be approximately 47 ms since the experiments are carried out at onstream velocities between U_∞ = 35.5 m/s and 39 m/s. Therefore, the expected value is slightly smaller than t = 60 ms. This is due to the fact that the time is counted from the initial movement of the vortex generator, while passing α_{vg} = -10°.

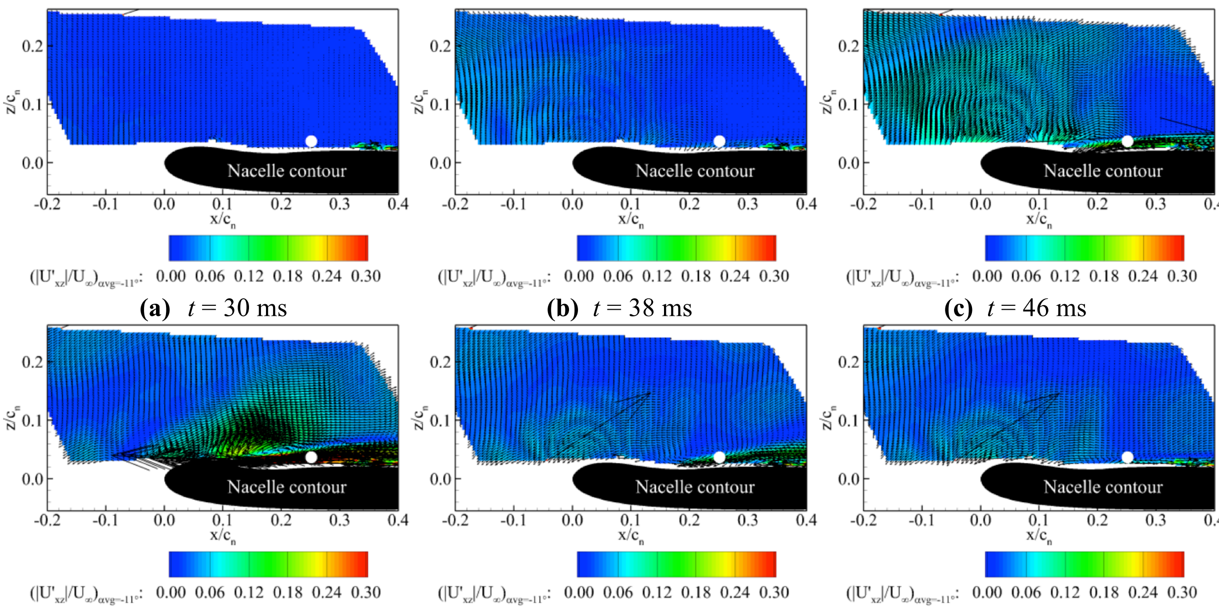

(a) t = 30 ms **(b)** t = 38 ms **(c)** t = 46 ms

(d) t = 54 ms **(e)** t = 62 ms **(f)** t = 70 ms

Fig. 13 Absolute in-plane fluctuation velocities at α_n = 19°

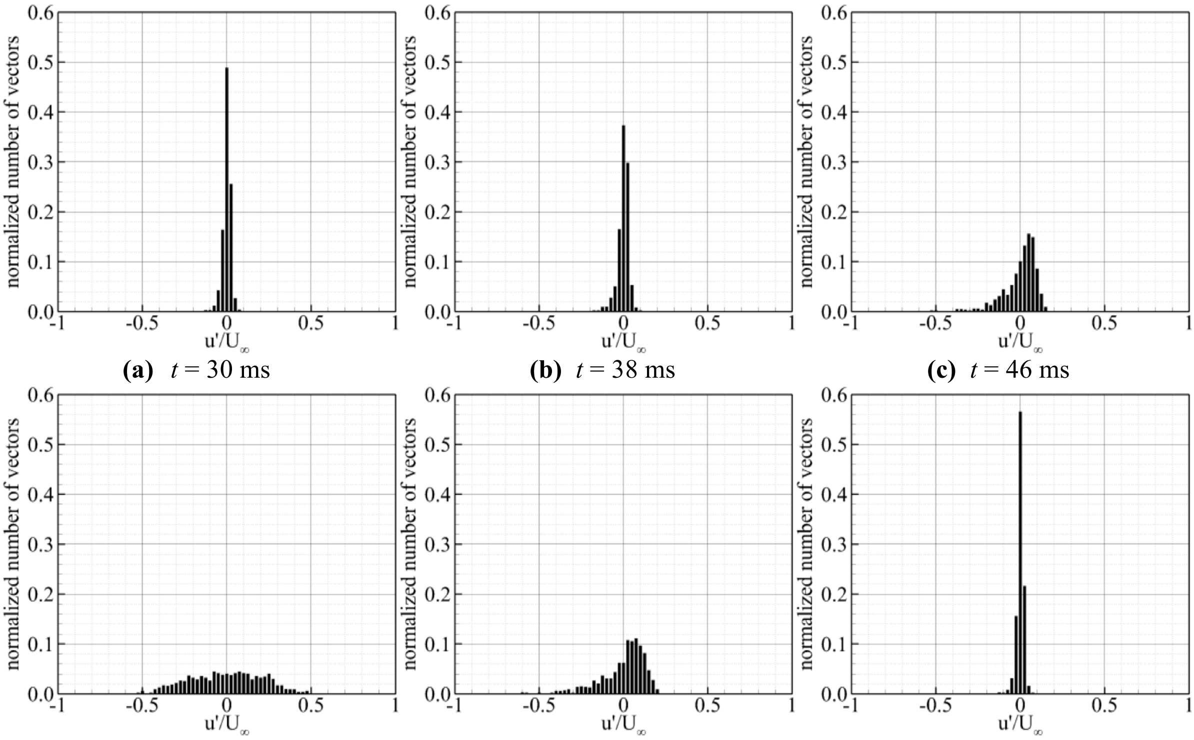

(a) $t = 30$ ms **(b)** $t = 38$ ms **(c)** $t = 46$ ms

(d) $t = 54$ ms **(e)** $t = 62$ ms **(f)** $t = 70$ ms

Fig. 14 Histograms of the normalized velocity fluctuation u'/U_∞ for different times t at $\alpha_n = 19°$

The almost symmetric irregularities in the vector fields in Figs. 7 and 8 are a consequence of strong reflections of the laser light on pressure sensors downstream of the light sheet. The real flow field is considered to be more homogenous than the one shown. Also, the two points of relatively low turbulent kinetic energy in the red region of Fig. 12 (b) underline the problem in the cross section.

Compared to the problems with the reflections during the PIV measurements in the cross section, the measurements in the section of the main flow direction lead to smooth distributions of statistical data, see Fig. 10.

In Fig. 13 an equidistant time series of vector fields of the interaction between the vortex and the nacelle is shown at $\alpha_n = 19°$. The black contour is the bottom leading edge of the nacelle, whereas the white point indicates the position where the histograms of the normalized velocity fluctuation u' are calculated, see Fig. 14. The colors in Fig. 13 indicate the absolute normalized in-plane velocity fluctuations given as

$$(|U'_{xz}|/U_\infty)_{\alpha_{vg}=-11°} = \sqrt{\left(u'_{\alpha_{vg}=-11°}/U_\infty\right)^2 + \left(w'_{\alpha_{vg}=-11°}/U_\infty\right)^2}. \tag{3}$$

While u' is the velocity fluctuation in the x-direction, w' is the velocity fluctuation in the z-direction. The index $\alpha_{vg} = -11°$ indicates that the vector field with the vortex generator at a steady angle of attack of -11° was subtracted from the correspondent phase averaged velocity field at time t. The vectors in Fig. 13 show the fluctuation velocities $u'_{\alpha vg = -11°}$ and $w'_{\alpha vg = -11°}$. The time spacing between the plotted vector fields is 8 ms. The influence of the counter clockwise rotating vortex on the flow field can be clearly seen in Figs. 13 (c) – 13 (e). The near-wall distortions are particularly high. Therefore, histograms of the fluctuation velocities u' were calculated in this area. Note that the histograms were calculated for the phase averaged fluctuation velocities. The number of vectors was normalized with the total number of vector fields (i.e. 1000). The bin-width was chosen as $u/U_\infty = 0.025$. Figure 14 shows that the fluctuation velocities are relatively small at $t = 30$ ms, $t = 38$ ms and $t = 70$ ms, whereas the fluctuations during the distortion at $t = 46$ ms - 62 ms are higher. The histograms in Figs. 14 (c) and 14 (e) show that the fluctuation velocities can also have an unbalanced distribution. The unbalanced as well as the broad distribution of the fluctuation velocities are an effect of the vortex. Therefore, this counter clockwise rotating vortex has a critical effect on the attached

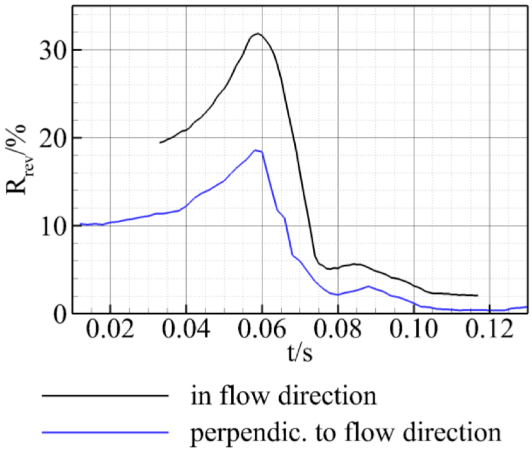

Fig. 15 Probability for reversed flow at α_n = 23°

flow in the nacelle as already shown above. These distortions can occur, while the airplane is flying with an attached inlet through gusty conditions.

The effect of the vortex generator on the separated flow has already been shown in Figs. 6, 8, 10 and 12. However, the effect of the vortex on the probability for reversed flow in the nacelle will be discussed below. Figure 15 shows the ratio of reversed vectors to the total amount of vectors from the leading edge of the nacelle to the edge of the field of view R_{rev} over the time. The black curve shows the result in the mid section in main flow direction of the nacelle, whereas the blue line shows the result for the cross section at $x/c_n = 0.2$. Therefore, the reason for the difference of the absolute values of R_{rev} lies in the observation of the different sections. However, it becomes apparent that the peak in both curves is at $t \approx 60$ ms. This value is higher than the expected convection velocity of the vortex due to the fact that the time is counted from the initial movement of the vortex generator and the vortex needs some time to develop. Figure 15 also shows that the amount of the reversed vectors is lower after the distortion than before. The reason for that is the induced velocity due to the vortex generator's airfoil at steady state according to the Biot-Savart law. While at $\alpha_{vg} = 11°$ the effective angle of attack of the nacelle is increased, the effective α_n is reduced at $\alpha_{vg} = 11°$. This phenomenon leads to a shift of separation onset. Therefore at $\alpha_{vg} = 11°$, separation onset is shifted towards higher angels of attack than at $\alpha_{vg} = -11°$. The shift of separation onset was shown in static pressure measurements. At $\alpha_n = 23°$, when a relatively big turbulent separation bubble has already formed, this effect leads to a decrease of the ratio of reversed flow R_{rev}, see Fig. 15.

Figure 16 shows the contour lines of the velocity $u/U_\infty = 0$ for different times t in the inlet. This zero velocity in the x-direction indicates the dynamics during the impingement of the vortex on the nacelle. The lines were derived from the SPIV results at each vector position. The result was filtered using a moving average with a span of 20. At $t = 40$ ms (blue line) the contour of zero velocity has a certain size, which increases up to $t = 60$ ms. The maximum extension in the radial direction is almost 10% of the nacelles chord, while the axial size of the contour line is approximately 40% of the chord at $\alpha_n = 23°$. The amount of reversed velocities decreases after $t = 60$ ms, as shown in Fig. 15. This also means that the contour line of zero

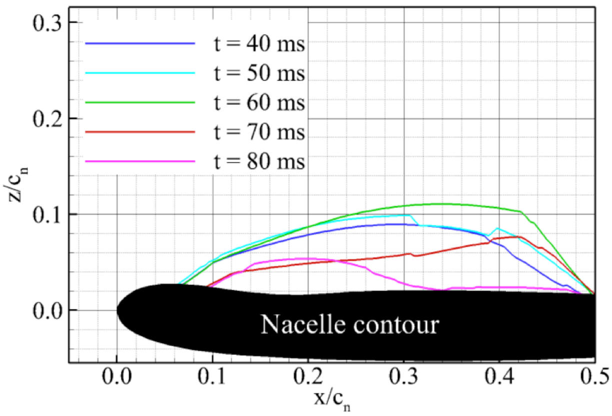

Fig. 16 Lines of $u/U_\infty = 0$ at α_n = 23°

velocities $u/U_\infty = 0$ decreases, see Fig. 16. Even the smaller ratio of reversed vectors after the interaction - shown in Fig. 15 - is reproduced by a smaller area of velocities $u/U_\infty < 0$ for $t = 80$ ms compared with $t = 40$ ms in Fig. 16. Additionally, a deformation of the red line of zero velocity can be discovered in Fig. 16.

4. Conclusion

SPIV measurements and time averaged static pressure measurements are presented in this paper. The motivation of these measurements was to investigate the effect of an atmospheric distortion on the attached as well as the separated flow in a nacelle. The experiments serve as a validation database in order to develop sophisticated numerical models to calculate the flow at the edge of the flight envelope. The measurements were performed at high angles of attack and low Reynolds numbers of $Re_{cn} \approx 1.25 \cdot 10^6$. The investigated model is a generic axially symmetric flow-through nacelle. The boundary layer loading of the nacelle is similar to that of a powered jet intake during take-off and landing and high mass flow rates, see Schulze (2013). Distortions are generated by a pitching airfoil in the test section upstream of the nacelle in order to simulate an atmospheric gust. These distortions are judged to have a critical effect on the inlet separation, as the turbulent separation bubble is increased in the axial and the radial direction by the interaction with the counter clockwise rotating vortex, see Fig. 6. This result was expected as the rotation of the vortex initially increases the angle of attack of the nacelle. The ratio of reversed vectors to all vectors in the SPIV field of view, downstream of the nacelle's leading edge, indicates that the region of reversed flow is primarily increased. After the interaction, the ratio of reversed vectors R_{rev} lies below the level before the impingement of the vortex. The velocity induced by the vortex generator's airfoil leads to a decrease of the region of reversed flow at the nacelle, see Figs. 15 and 16. Investigations of experiments with attached flow in the nacelle at $\alpha_n = 19°$ indicate that the generated distortion has a crucial effect as well. Fluctuation velocities in the near-wall region are increased while the vortex interacts with the nacelle, see Fig. 14.
It can be concluded that the vortex generator is adequately constructed to disturb the flow field in this model significantly. The vortex is convected with the free stream velocity of the wind tunnel. The validation of the unsteady pressure measurements, as well as the time resolved SPIV validation, will show if the vortex shedding is influenced by the distortion as well. Furthermore, the effect of the clockwise rotating vortex on the flow has to be investigated.

Acknowledgments

The authors would like to thank the Deutsche Forschungsgemeinschaft for founding the research within the framework of the research group 1066 “Simulation of wing and nacelle stall”.

References

- Hahn D, Scholz P, Radespiel R (2012) Vortex Generation in a low speed wind tunnel and vortex interactions with a high-lift airfoil. 30th AIAA Applied Aerodynamics Conference, doi: 10.2514/6.2012-3024, New Orleans, Louisiana.
- Niehuis R, Lesser A, Probst A, Radespiel R, Schulze S, Kähler CJ, Spiering F, Kroll N, Wartzek F, Schiffer H-P (2013) Simulation of Nacelle Stall and Engine Response. Proceedings of the XXI. International Symposium on Air Breathing Engines (ISABE), Busan, Korea.
- Radespiel R, Gisele Francois D, Hoppermann D, Klein S, Scholz P, Wawrzinek K, Lutz T, Auerswald T, Bange J, Knigge C, Raasch S, Kelleners P, Heinrich R, Reuß S, Probst A, Knopp T (2013) Simulation of Wing Stall. 43rd AIAA Fluid Dynamics Conference, doi: 10.2514/6.2013-3175, San Diego, California.
- Schulze S, Kähler CJ, and Radespiel R (2007) On the Comparison of Stalling Flow-Through Nacelles and Powered Inlets at Take-Off Conditions. 1st CEAS European Air and Space Conference, Berlin, Germany.
- Schulze S (2013) Experimentelle Untersuchungen zur Wirbeldynamik am überziehenden Triebwerkseinlauf. Shaker Verlag, Aachen, Germany.
- Vollmers H (2001) Detection of vortices and quantitative evaluation of their main parameters from experimental velocity data. Meas Sci Technol, 12:1199-1207.